

# FireFlow: Fast Inversion of Rectified Flow for Image Semantic Editing

Yingying Deng<sup>\*</sup> Xiangyu He<sup>\*1</sup> Changwang Mei<sup>1</sup> Peisong Wang<sup>1</sup> Fan Tang<sup>2</sup>



Figure 1. FireFlow for Image Inversion and Editing in 8 Steps. Our approach achieves outstanding results in semantic image editing and stylization guided by prompts, while maintaining the integrity of the reference content image and avoiding undesired alterations. [+] / [-] means adding or removing contents, [C] indicates changes in visual attributes (style, material, or texture), and [R] denotes content or gesture replacements.

## Abstract

Though Rectified Flows (ReFlows) with distillation offers a promising way for fast sampling, its fast inversion transforms images back to structured noise for recovery and following editing remains unsolved. This paper introduces FireFlow, a simple yet effective zero-shot approach that inherits the startling capacity of ReFlow-based models (such as FLUX) in generation while extending its capabilities to accurate inversion and editing in 8 steps. We first demonstrate that a carefully designed numerical solver is pivotal for ReFlow inversion, enabling accurate inversion

and reconstruction with the precision of a second-order solver while maintaining the practical efficiency of a first-order Euler method. This solver achieves a  $3\times$  runtime speedup compared to state-of-the-art ReFlow inversion and editing techniques, while delivering smaller reconstruction errors and superior editing results in a training-free mode. The code is available at [this URL](#).

## 1. Introduction

The ability to accurately and efficiently invert generative models is critical for enabling applications such as semantic image editing, data reconstruction, and latent space manipulation. Inversion, which involves mapping observed data back to its latent representation, serves as the foundation for fine-grained control over generative processes. Achieving a balance between computational efficiency and numerical accuracy in inversion is particularly challenging for diffusion

<sup>\*</sup>Equal contribution <sup>1</sup>Institute of Automation, Chinese Academy of Sciences, Beijing, China <sup>2</sup>Institute of Computing Technology, Chinese Academy of Sciences, Beijing, China. Correspondence to: Xiangyu He <hexiangyu17@mails.ucas.edu.cn>.

models, which rely on iterative processes to bridge data and latent spaces.

Diffusion models have long been regarded as the gold standard for high-quality data generation (Ramesh et al., 2022; Rombach et al., 2022; Podell et al., 2024) and inversion due to their ability to capture complex distributions through stochastic differential equations (SDEs). Their success has often overshadowed deterministic approaches such as Rectified Flow (ReFlow) models (Liu et al., 2023), which replace stochastic sampling with ordinary differential equations (ODEs) for faster and more efficient transformations. Despite skepticism about their capabilities, ReFlow models have demonstrated competitive generative performance, with the FLUX model (Forest) emerging as a leading open-source example. FLUX achieves remarkable instruction-following capabilities, challenging the assumption that diffusion models are inherently superior. These advances motivate a closer investigation of ReFlow-based models, particularly in the context of inversion and editing, to develop simple and effective methods.

ReFlow models possess an underutilized advantage: a well-trained ReFlow model learns nearly constant velocity dynamics across the data distribution, ensuring stability and bounded velocity approximation errors. However, existing inversion methods for ReFlow models fail to fully exploit this property. Current approaches rely on generic Euler solvers that prioritize each step’s computational efficiency at the expense of accuracy or incur additional costs to achieve higher precision. As a result, the potential of ReFlow models to deliver fast and accurate inversion remains untapped.

In this work, we introduce a novel numerical solver for the ODEs underlying ReFlow models, addressing the challenges of inversion and editing. Our method achieves second-order precision while retaining the computational cost of a first-order solver. By reusing intermediate velocity approximations, our approach reduces redundant evaluations, stabilizes the inversion process, and fully leverages the constant velocity property of well-trained ReFlow models. As shown in Table 1, our approach is the first to provide a solver that strikes an optimal trade-off between accuracy and efficiency, enabling ReFlow models to excel in inversion and editing tasks. By combining computational efficiency, numerical robustness, and simplicity, our method offers a scalable solution for real-world tasks requiring high fidelity and real-time performance, advancing the utility of ReFlow-based generative models like FLUX.

## 2. Preliminaries and related works

### 2.1. Rectified Flow

Rectified Flow (Liu et al., 2023) offers a principled approach for modeling transformations between two distributions,  $\pi_0$

Table 1. Comparison of recent training-free inversion and editing methods based on FLUX, including inversion/denoising steps, NFEs (Number of Function Evaluations) for both inversion and editing, local truncation error orders for solving ODE, and the need for a pre-trained auxiliary model for editing. Our approach offers a simple yet effective solution to address the challenges.

Methods	Add-it	RF-Solver	RF-Inv.	Ours
<b>Steps</b>	30	15	28	8
<b>NFE</b>	60	60	56	18
<b>Aux. Model</b>	✓	w/o	w/o	w/o
<b>Local Error</b>	$\mathcal{O}(\Delta t^2)$	$\mathcal{O}(\Delta t^3)$	$\mathcal{O}(\Delta t^2)$	$\mathcal{O}(\Delta t^3)$

(Tewel et al., 2024) for Add-it, (Wang et al., 2024) for RF-Solver, (Rout et al., 2024) for RF-Inv.

and  $\pi_1$ , based on empirical observations  $X_0 \sim \pi_0$  and  $X_1 \sim \pi_1$ . The transformation is represented as an ordinary differential equation (ODE) over a continuous time interval  $t \in [0, 1]$ :

$$dZ_t = v(Z_t, t) dt, \quad (1)$$

where  $Z_0 \sim \pi_0$  is initialized from the source distribution, and  $Z_1 \sim \pi_1$  is generated at the end of the trajectory. The drift  $v : \mathbb{R}^d \times [0, 1] \rightarrow \mathbb{R}^d$  is designed to align the trajectory of the flow with the direction of the linear interpolation path between  $X_0$  and  $X_1$ . This alignment is achieved by solving the following least squares regression problem:

$$\min_v \mathbb{E} \left[ \int_0^1 \|(X_1 - X_0) - v_\theta(X_t, t)\|_2^2 dt \right], \quad (2)$$

where  $X_t = tX_1 + (1-t)X_0$  denotes the linear interpolation path between  $X_0$  and  $X_1$ .

**Forward process** seeks to transform samples  $X_0 \sim \pi_0$  to match the target distribution  $\pi_1$ . A direct parameterization of  $X_t$  is given by the linear interpolation  $X_t = tX_1 + (1-t)X_0$ , which satisfies the non-causal ODE:

$$dX_t = (X_1 - X_0) dt. \quad (3)$$

However, this formulation assumes prior knowledge of  $X_1$ , rendering it non-causal and unsuitable for practical simulation. By introducing the drift  $v(X_t, t)$ , rectified flow causalizes the interpolation process. The drift  $v$  is fit to approximate the linear direction  $X_1 - X_0$ , resulting in the forward ODE with  $X_0 \sim \pi_0$ :

$$dX_t = v(X_t, t) dt, \quad t \in [0, 1]. \quad (4)$$

This causalized forward process enables simulation of  $Z_t$  without requiring access to  $X_1$  during intermediate time steps.

**Reverse process** generates samples from  $\pi_1$  by reversing the learned flow. Starting from  $X_1 \sim \pi_1$ , the reverse ODE is given by negating the drift term:

$$dX_t = -v(X_t, t) dt, \quad t \in [1, 0]. \quad (5)$$

This process effectively “undoes” the transformations applied during the forward flow, enabling the generation of  $X_0$  that follows the original distribution  $\pi_0$ . The reverse process guarantees consistency with the forward dynamics by leveraging the symmetry of the learned drift  $v$ .

## 2.2. Inversion

The inversion of real images into noise feature space, as well as the reconstruction of noise features back to the original real images, is a prominent area of research within diffusion models applied to image editing tasks (Lin et al., 2024; Brack et al., 2024; Miyake et al., 2023; Ju et al., 2024; Zhang et al., 2022; Huberman-Spiegelglas et al., 2024; Cho et al., 2024). The foundational theory of Denoising Diffusion Implicit Models (DDIM) (Song et al., 2021) involves the addition of predicted noise to a fixed noise during the forward process, which can subsequently be mapped to generate an image. However, this approach encounters challenges related to reconstruction bias. To address this issue, Null-Text Inversion (Mokady et al., 2023) optimizes an input null-text embedding, thereby correcting reconstruction errors at each iterative step. Similarly, Prompt-Tuning-Inversion (Dong et al., 2023) refines conditional embeddings to accurately reconstruct the original image. Negative-Prompt-Inversion (Miyake et al., 2023) replaces the null-text embedding with prompt embeddings to expedite the inversion process. Direct-Inversion (Ju et al., 2024) incorporates the inverted noise corresponding to each timestep within the denoising process to mitigate content leakage.

In contrast to the aforementioned Stochastic Differential Equation (SDE)-based formulations, rectified flow models that utilize ordinary differential equations (ODEs) offer a more direct solution pathway. RF Inversion (Rout et al., 2024) employs dynamic optimal control techniques derived from linear quadratic regulators, while RF-Solver (Wang et al., 2024) utilizes Taylor expansion to minimize inversion errors in ODEs. Nevertheless, achieving superior inversion results typically necessitates an increased number of generation steps, which can lead to significant computational time and resource expenditure. In this paper, we propose a few-step ODE solver designed to balance effective outcomes with high efficiency.

## 2.3. Editing

Image editing utilizing a pre-trained diffusion model has demonstrated promising results, benefiting from advancements in image inversion and attention manipulation technologies (Hertz et al., 2022; Cao et al., 2023; Meng et al., 2022; Couairon et al., 2023a; Deutch et al., 2024; Xu et al., 2024; Brooks et al., 2023). Training-free editing methods typically employ a dual-network architecture: one network

is dedicated to reconstructing the original image, while the other is focused on editing. The Prompt-to-Prompt (Hertz et al., 2022) approach manipulates the cross-attention maps within the editing pipeline by leveraging features from the reconstruction pipeline. The Plug-and-Play (Tumanyan et al., 2023a) method substitutes the attention matrices of self-attention blocks in the editing pipeline with those from the reconstruction pipeline. Similarly, MasaCtrl (Cao et al., 2023) modifies the Value components of self-attention blocks in the editing pipeline using values derived from the reconstruction pipeline. Additionally, the Add-it (Tewel et al., 2024) method utilizes both the Key and Value components of self-attention blocks from the source image to guide the editing process effectively.

## 3. Motivation

The ReFlow model operates under the simple assumption that  $X_t$  evolves linearly between  $X_0$  and  $X_1$ , corresponding to uniform linear motion. Drawing an analogy to physics, it is natural to extend this linear motion to accelerated motion by incorporating an acceleration term:

$$\frac{dv_t}{dt} = a(X_t, t), \quad \frac{dX_t}{dt} = v(X_t, t), \quad (6)$$

where  $X_{t+1} = X_t + v_t \Delta t + \frac{1}{2} a_t \Delta t^2$ , and  $v_t$  is equivalent to  $v(X_t, t)$  for simplicity. Recent works have empirically shown that training-based strategies (Park et al., 2024; Chen et al., 2024) for solving Equation (6) improve coupling preservation and inversion over rectified flow, even with few steps. Moreover, a training-free method (Wang et al., 2024) leveraging pre-trained ReFlow models has also demonstrated the utility of the second-order derivative of  $v$  in achieving effective inversion, essentially aligning with the principles of accelerated motion.

However, this observation appears counterintuitive. A well-trained ReFlow model, such as FLUX, generally assumes that  $v_t$  approximates the constant value  $X_1 - X_0$ . Thus, the acceleration term  $a_t = dv_t/dt$  theoretically approaches zero, as the learning target for  $v_t$  is constant.

**Connection to High-Order ODE Solvers:** Instead of treating  $a_t$  as a continuous term, we reinterpret it through the lens of high-order ODE solvers. Using the finite-difference approximation  $a_t = (v_{t+\Delta t} - v_t)/\Delta t$ , we can rewrite the equation as:

$$X_{t+1} = X_t + v_t \Delta t + \frac{1}{2} a_t \Delta t^2 = X_t + \frac{1}{2} (v_t + v_{t+\Delta t}) \Delta t,$$

which corresponds to the standard formulation of the second-order Runge-Kutta method. This high-order approach allows fewer steps (or equivalently, larger step sizes  $\Delta t$ ) to achieve the same accuracy as Euler’s method, since the global error of a  $p$ -th order method scales as  $\mathcal{O}(\Delta t^p)$ .

This enables larger  $\Delta t$  while maintaining the same error tolerance  $\epsilon$ . Similarly, if we approximate  $a_t$  using  $a_t = (v_{t+\frac{1}{2}\Delta t} - v_t)/(\frac{1}{2}\Delta t)$ , the resulting position update becomes:

$$X_{t+1} = X_t + v_{t+\frac{1}{2}\Delta t}\Delta t,$$

which corresponds to the standard midpoint method, another second-order ODE solver.

**Impact on ReFlow Inversion:** It is well-established that the global error in the forward process of ODE solvers benefits from higher-order methods. Likewise, inversion and reconstruction tasks also exhibit improved performance with high-order solvers, as they better preserve original image details during the inversion of ReFlow models. We formalize this property in the following statement.

**Proposition 3.1.** *Given a  $p$ -th order ODE solver and the ODE  $\frac{dX_t}{dt} = v_\theta(X_t, t)$ , if the dynamics of the reverse pass satisfy  $\frac{dX_t}{dt} = -v_\theta(X_t, t)$  which is Lipschitz continuous with constant  $L$ . The perturbation  $\Delta_T$  at  $t = T$  propagates backward to  $t = 0$ . The propagated error satisfies:*

$$\|\Delta_0\| \leq e^{-LT} \|\Delta_T\|. \quad (7)$$

**Implication.** The inversion error  $\|\Delta_T\|$  introduced during the  $p$ -th order numerical solution propagates into the reverse pass, experiencing a slight reduction scaled by the Lipschitz constant  $L$  of the learned drift  $v_\theta(X_t, t)$ . Despite this reduction, the overall reconstruction error  $\|\Delta_0\|$  for the original image remains asymptotically of the same order,  $\mathcal{O}(\Delta t^p)$ , where  $\Delta t$  represents the integration step size. Consequently, high-order solvers are preferred in ReFlow to achieve accurate inversion and editing with fewer steps.

## 4. Method

**Challenges with High-Order Solvers:** While the use of high-order solvers is theoretically promising, it fails to yield practical runtime speedups. For a parameterized drift  $v_\theta(X_t, t)$ , the runtime is determined by the Number of Function Evaluations (NFEs), i.e., the number of forward passes through the model  $v_\theta(X_t, t)$ . High-order solvers require evaluating more points within the interval  $[t, t + 1]$ , leading to a higher NFE per step, which negates any reduction in the number of steps and fails to improve overall computational efficiency.

For instance, the midpoint method achieves a local error of  $\mathcal{O}(\Delta t^3)$  and a global error of  $\mathcal{O}(\Delta t^2)$ . Formally, it proceeds as follows:

$$X_{t+\frac{\Delta t}{2}} = X_t + \frac{\Delta t}{2} v_\theta(X_t, t), \quad (8)$$

$$X_{t+1} = X_t + \Delta t \cdot v_\theta\left(X_{t+\frac{\Delta t}{2}}, t + \frac{\Delta t}{2}\right). \quad (9)$$

This scheme requires two NFEs per step: one to compute  $X_{t+\frac{\Delta t}{2}}$  and another for  $v_\theta\left(X_{t+\frac{\Delta t}{2}}, t + \frac{\Delta t}{2}\right)$ , effectively doubling the cost compared to the Euler method. The midpoint method leverages  $v_{t+\frac{\Delta t}{2}}$  to provide a more accurate estimate of  $\frac{X_{t+1}-X_t}{\Delta t}$  than  $v_t$ , which inspires us to seek an alternative with lower computational cost.

**A Low-Cost Alternative:** The training objective of ReFlow implies that a well-trained model satisfies  $v_\theta(X_t, t) \approx (X_1 - X_0)$  for all  $t$ . Leveraging this property, the most efficient approach would replace  $v_t$  with  $v_0$ , enabling one-step generation as proposed in the original ReFlow method (Liu et al., 2023). However, this simplification makes it difficult to incorporate conditional priors, as multi-step iteration is no longer required.

To maintain a multi-step paradigm, we propose a modified scheme that replaces  $v_t$  with previous  $t - 1$ -step midpoint velocity  $v_{(t-1)+\frac{\Delta t}{2}}$  rather than  $v_{t+\frac{\Delta t}{2}}$ . This approach is formalized as:

$$\hat{v}_\theta(X_t, t) := \underbrace{v_\theta\left(X_{(t-1)+\frac{\Delta t}{2}}, (t-1) + \frac{\Delta t}{2}\right)}_{\text{load from memory}} \quad (10)$$

$$\hat{X}_{t+\frac{\Delta t}{2}} := X_t + \frac{\Delta t}{2} \hat{v}_\theta(X_t, t) \quad (11)$$

$$X_{t+1} = X_t + \Delta t \cdot \underbrace{v_\theta\left(\hat{X}_{t+\frac{\Delta t}{2}}, t + \frac{\Delta t}{2}\right)}_{\text{run \& save to memory}} \quad (12)$$

In this scheme, only one NFE is required per step<sup>1</sup>, matching the computational cost of the Euler method. The key question, then, is whether this scheme retains the second-order accuracy of the original midpoint method.

For the local and global truncation error, we derive that if  $v_\theta(X_t, t)$  is well-trained and varies smoothly with respect to both  $X$  and  $t$ , the proposed scheme achieves the same truncation error as the standard midpoint method. This ensures that the modified approach retains the benefits of second-order accuracy while operating at the computational cost of a first-order solver.

**Proposition 4.1.** *Let  $\hat{v}_\theta(X_t, t)$  denote the reused velocity approximation in Equation 10, and  $v_\theta(X_t, t)$  denotes the exact velocity at time  $t$ . Then, the approximation satisfies the error bound:  $\|\hat{v}_\theta(X_t, t) - v_\theta(X_t, t)\| \leq \mathcal{O}(\Delta t)$ , under the following conditions:*

1) *Temporal Error: The temporal error is directly proportional to the time step  $\Delta t$ , stemming from smoothness of  $v_\theta(X, t)$  in the time domain.*

2) *Spatial Error: The spatial error is dominated by  $\mathcal{O}(\Delta t)$ ,*

<sup>1</sup>Specifically, we perform two NFEs at  $t = 0$  to initialize the conditions  $v_0$  and  $v_{0+\frac{\Delta t}{2}}$  for subsequent iterations. Python-style pseudo-code is provided in Sec.D.

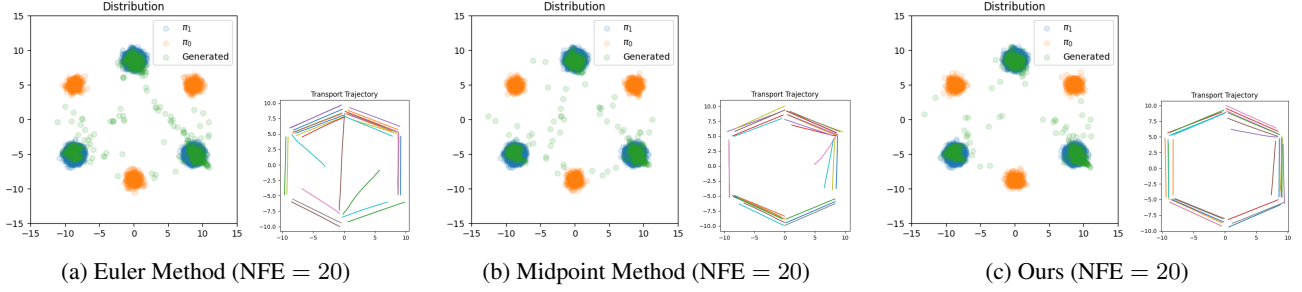


Figure 2. Results on 2D synthetic dataset. We evaluate the performance of 2-Rectified Flow using the Euler solver, midpoint solver, and our proposed approach on a 2D synthetic dataset. The source distribution  $\pi_0$  (orange) and the target distribution  $\pi_1$  (green) are parameterized as Gaussian mixture models. For the Euler method, the number of sampling steps is set to  $N = 20$ , corresponding to an NFE of 20. Our approach generates samples that align more closely with the target distribution, achieving a better match in density and structure. Additionally, the trajectories of the samples exhibit greater straightness, adhering closely to the ideal of linear motion.

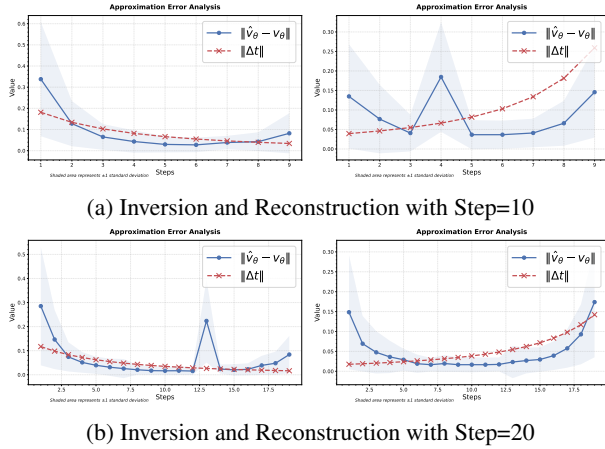


Figure 3. Illustrations of the approximation error in velocity ( $\|\hat{v}_\theta - v_\theta\|$ ) as it evolves with inversion steps (left subfigures) and denoising steps (right subfigures), with  $\Delta t$  included as a reference.

due to the boundedness of  $\frac{\partial v_\theta}{\partial X}$ .

We formally prove in the appendix that when two required conditions are satisfied, leading to the following result: our modified midpoint method achieves the same truncation error as the standard midpoint method under these circumstances. Consequently, it is expected to exhibit smaller overall error while maintaining the same runtime cost as the first-order Euler method.

**Theorem 4.2.** Consider a ReFlow model governed by ODE:  $\frac{dX}{dt} = v_\theta(X, t)$ , where  $v_\theta(X, t)$  is smooth and bounded, and the solution  $X_t$  evolves over a time interval  $[0, T]$ . The modified midpoint method, defined in Equation (12), achieves the same global truncation error  $\mathcal{O}(\Delta t^2)$  as the standard midpoint method, provided the reused velocity satisfies:  $\|\hat{v}_\theta(X_t, t) - v_\theta(X_t, t)\| \leq \mathcal{O}(\Delta t)$ .

To highlight the advantages of our approach, we conduct experiments on synthetic data following the setup in (Liu

et al., 2023). As shown in Figure 2, the transport trajectories generated by our method are straighter, leading to improved accuracy while maintaining the same NFE as the Euler method, and even surpassing the performance of the standard midpoint method.

**Numerical Results and Discussion** To empirically validate the theoretical assumption that the reused velocity approximation error  $\|\hat{v}_\theta(X_t, t) - v_\theta(X_t, t)\|$  is bounded by  $\mathcal{O}(\Delta t)$ , we conducted numerical experiments and analyzed the relationship between the approximation error and the time step size  $\Delta t$  on FLUX-dev model during inversion and reconstruction. The results are summarized in Figure 3, which depicts the average approximation error across different step sizes, with the shaded area representing  $\pm 1$  standard deviation.

The data exhibit the following key trend that the approximation error grows approximately linearly with the step size  $C \cdot \Delta t$ , consistent with the theoretical bound  $\mathcal{O}(\Delta t)$ . Despite the inherent variability of the error (illustrated by the shaded standard deviation), the magnitude of the error remains well-controlled and stable across most steps, further validating the robustness of the reused velocity approximation in practice.

**Image Semantic Editing:** To ensure simplicity and fairness in comparison with other methods, we adopt the approach in (Wang et al., 2024), where the value features in self-attention layers during the denoising process are replaced with pre-stored value features generated during the inversion process, serving as a prior. Subsequently, a reference prompt is used as guidance to achieve semantic editing. Leveraging the superior image preservation of our numerical solver, our method does not require careful selection of timesteps or specific blocks for applying the replacements in self-attention layers, as suggested in the original paper. Instead, we uniformly apply this strategy to all self-attention layers solely at the first denoising step, which we find em-

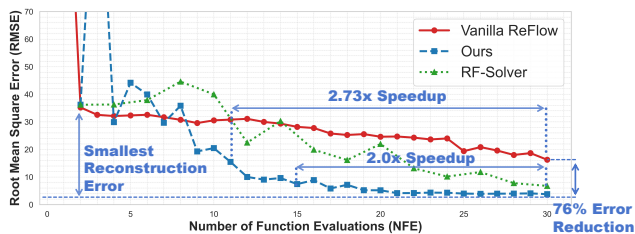


Figure 4. Image reconstruction errors versus denoising NFE: Our approach, compared to the first-order vanilla ReFlow inversion and second-order RF-solver, achieves lower reconstruction errors and demonstrates faster convergence with respect to NFE.

pirically effective. The inversion and denoising sampling processes are detailed in Algorithms 1 and 2.

## 5. Experiment

### 5.1. Implementation Details

**Baselines:** This section compares FireFlow with DM inversion-based editing methods such as Prompt-to-Prompt (Hertz et al., 2022), MasaCtrl (Cao et al., 2023), Pix2Pix-zero (Parmar et al., 2023), Plug-and-Play (Tumanyan et al., 2023a), DiffEdit (Couairon et al., 2023b) and DirectInversion (Ju et al., 2024). We also consider the recent RF inversion methods, such as RF-Inversion (Rout et al., 2024) and RF-Solver (Wang et al., 2024).

**Metrics:** We evaluate different methods across three aspects: generation quality, text-guided quality, and preservation quality. The Fréchet Inception Distance (FID) (Heusel et al., 2017) is used to measure image generation quality by comparing the generated images to real ones. A CLIP model (Radford et al., 2021) is used to calculate the similarity between the generated image and the guiding text. To assess the preservation quality of non-edited areas, we use metrics including Learned Perceptual Image Patch Similarity (LPIPS) (Zhang et al., 2018), Structural Similarity Index Measure (SSIM) (Wang et al., 2004), Peak Signal-to-Noise Ratio (PSNR), and structural distance (Ju et al., 2024).

**Steps:** Since the number of inference steps can significantly impact performance, we follow the best settings reported for the RF-Solver to ensure a fair comparison: 10 steps for text-to-image generation (T2I) and 30 steps for reconstruction. For editing, RF-Solver varies the number of steps by task, using up to 25 steps. In contrast, we find that our approach achieves comparable or better results using 8 steps. The ablation study is shown in Section E.

### 5.2. Text-to-image Generation

We compare the performance of our method against the vanilla rectified flow and the second-order RF-solver on the

Table 2. Quantitative results on Text-to-Image Generation.

Methods	FLUX-dev	RF-Solver	Ours
<b>Steps</b>	20	10	10
<b>NFE (↓)</b>	20	20	11
<b>FID (↓)</b>	26.77	25.93	<b>25.16</b>
<b>CLIP Score (↑)</b>	<b>31.44</b>	31.35	31.42
<b>ODE Solver</b>	1st-order	2nd-order	2nd-order

Table 3. Quantitative results for inversion and reconstruction using the FLUX-dev model (excluding the DDIM baseline). NFE includes both inversion and reconstruction function evaluations. Steps or computational costs are kept comparable across comparisons. **Reconstruction is performed without leveraging latent features from the inversion process.**

	Steps	NFE↓	LPIPS↓	SSIM↑	PSNR↑
DDIM-Inv.	50	100	0.2342	0.5872	19.72
RF-Solver	30	120	0.2926	0.7078	20.05
ReFlow-Inv.	30	60	0.5044	0.5632	16.57
Ours	30	62	<b>0.1579</b>	<b>0.8160</b>	<b>23.87</b>
RF-Solver	5	20	0.5010	0.5232	14.72
ReFlow-Inv.	9	18	0.8145	0.3828	15.29
Ours	8	18	<b>0.4111</b>	<b>0.5945</b>	<b>16.01</b>

fundamental T2I task. Following the setup in RF-solver, we evaluate a randomly selected subset of 10K images from the MSCOCO Caption 2014 validation set (Chen et al., 2015), using the ground-truth captions as reference prompts. The FID and CLIP scores for results generated with a fixed random seed of 1024 are presented in Table 2. In summary, our method delivers superior image quality while maintaining comparable text alignment performance.

### 5.3. Inversion and Reconstruction

**Quantitative Comparison:** We report the inversion and reconstruction results on the first 1K images from the Densely Captioned Images (DCI) dataset (Urbanek et al., 2024), using the official descriptions as source prompts. The results, shown in Table 3, demonstrate that our approach achieves a significant reduction in reconstruction error, whether compared at the same number of steps (yielding approximately  $2\times$  speedup) or at the same computational cost.

**Qualitative Comparison:** As shown in Figure 5, our approach provides an efficient and effective reconstruction method based on FLUX. The drift from the source image is significantly smaller compared to baseline methods, aligning with the quantitative results.

**Convergence Rate:** We empirically compare the convergence rates of different numerical solvers during reconstruction, as shown in Figure 4. For a fair comparison, we use the demo “boy” image and prompt provided in the RF-solver

Table 4. Compare our approach with other editing methods on PIE-Bench.

Method	Model	Structure	Background Preservation		CLIP Similarity $\uparrow$		Steps	NFE $\downarrow$
		Distance $\downarrow$	PSNR $\uparrow$	SSIM $\uparrow$	Whole	Edited		
Prompt2Prompt (Hertz et al., 2022)	Diffusion	0.0694	17.87	0.7114	25.01	22.44	50	100
Pix2Pix-Zero (Parmar et al., 2023)	Diffusion	0.0617	20.44	0.7467	22.80	20.54	50	100
MasaCtrl (Cao et al., 2023)	Diffusion	0.0284	22.17	0.7967	23.96	21.16	50	100
PnP (Tumanyan et al., 2023b)	Diffusion	0.0282	22.28	0.7905	25.41	22.55	50	100
PnP-Inv. (Ju et al., 2024)	Diffusion	<b>0.0243</b>	22.46	0.7968	25.41	22.62	50	100
RF-Inversion (Rout et al., 2024)	ReFlow	0.0406	20.82	0.7192	25.20	22.11	28	56
RF-Solver (Wang et al., 2024)	ReFlow	0.0311	22.90	0.8190	<u>26.00</u>	22.88	15	60
Ours	ReFlow	0.0283	<b>23.28</b>	<b>0.8282</b>	25.98	<b>22.94</b>	15	32
Ours	ReFlow	<u>0.0271</u>	<u>23.03</u>	<u>0.8249</u>	<b>26.02</b>	22.81	<b>8</b>	<b>18</b>

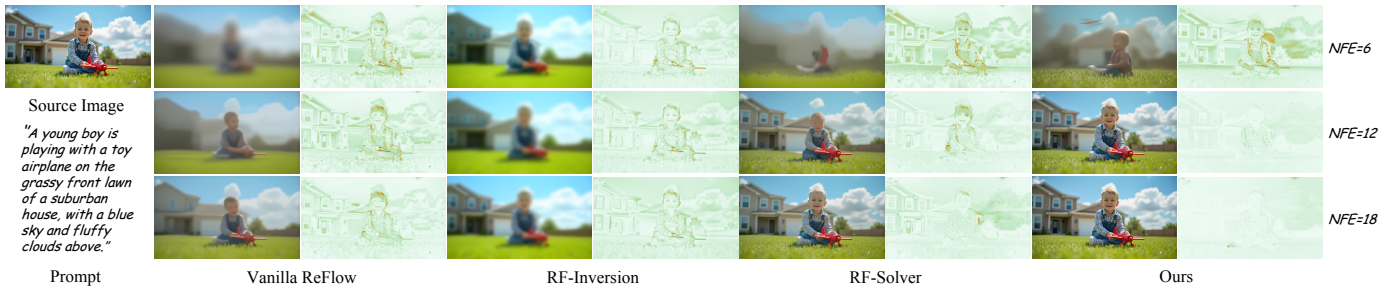


Figure 5. Qualitative results of image reconstruction. Our approach achieves faster convergence and superior reconstruction quality compared to baseline ReFlow methods utilizing the FLUX model. Difference images showing the pixel-wise variations between the source image and the reconstructed images are also provided.

source code. Our approach achieves the lowest reconstruction error with the fastest convergence rate, offering up to  $2.7\times$  speedup and over 70% error reduction. Figure 7 further illustrates the results when other approaches are fully converged at NFE = 120.

#### 5.4. Inversion-based Semantic Image Editing

**Quantitative Comparison:** We evaluate prompt-guided editing using the recent PIE-Bench dataset (Ju et al., 2024), which comprises 700 images across 10 types of edits. As shown in Table 4, we compare the editing performance in terms of preservation ability and CLIP similarity. Our method not only competes with but often outperforms other approaches, particularly in CLIP similarity. Notably, our approach achieves high-quality results with relatively few editing steps, demonstrating its efficiency and effectiveness in maintaining the integrity of the original content while producing edits that closely align with the intended modifications.

**Qualitative Comparison:** We present the visual editing results in Figure 6, which are consistent with our quantitative findings. Our method highlights a fundamental trade-off between minimizing changes to non-editing areas and enhancing the fidelity of the edits. In contrast, methods like P2P, Pix2Pix-Zero, MasaCtrl, and PnP often struggle with

Table 5. Per-image inference time for ReFlow inversion-based editing measured on an RTX 3090. The baseline is a vanilla ReFlow model utilizing 28 steps for both inversion and denoising.

	Resolution	Time Cost	Speedup
Vanilla ReFlow	512 $\times$ 512	23.76s	1.0 $\times$
RF-Inversion	512 $\times$ 512	23.36s	1.02 $\times$
RF-Solver	512 $\times$ 512	25.31s	0.94 $\times$
Ours	512 $\times$ 512	<b>7.70s</b>	<b>3.09<math>\times</math></b>
Vanilla ReFlow	1024 $\times$ 1024	72.10s	1.0 $\times$
RF-Inversion	1024 $\times$ 1024	71.35s	1.01 $\times$
RF-Solver	1024 $\times$ 1024	78.80s	0.92 $\times$
Ours	1024 $\times$ 1024	<b>24.52s</b>	<b>2.94<math>\times</math></b>

inconsistencies relative to the source image, as evident in the 3rd and 6th rows of the figure. Additionally, these methods frequently produce invalid edits, as shown in the 7th and 9th rows. While PnP-Inv excels at preserving the structure of the source image, it often fails to effectively apply the desired edits. Rectified flow model-based methods, such as RF-Inversion and RF-Solver, deliver better editing results compared to the aforementioned methods. However, they still face challenges with inconsistencies in non-editing areas. Overall, our method provides a more effective solution to these challenges, achieving superior results in both preservation and editing fidelity.

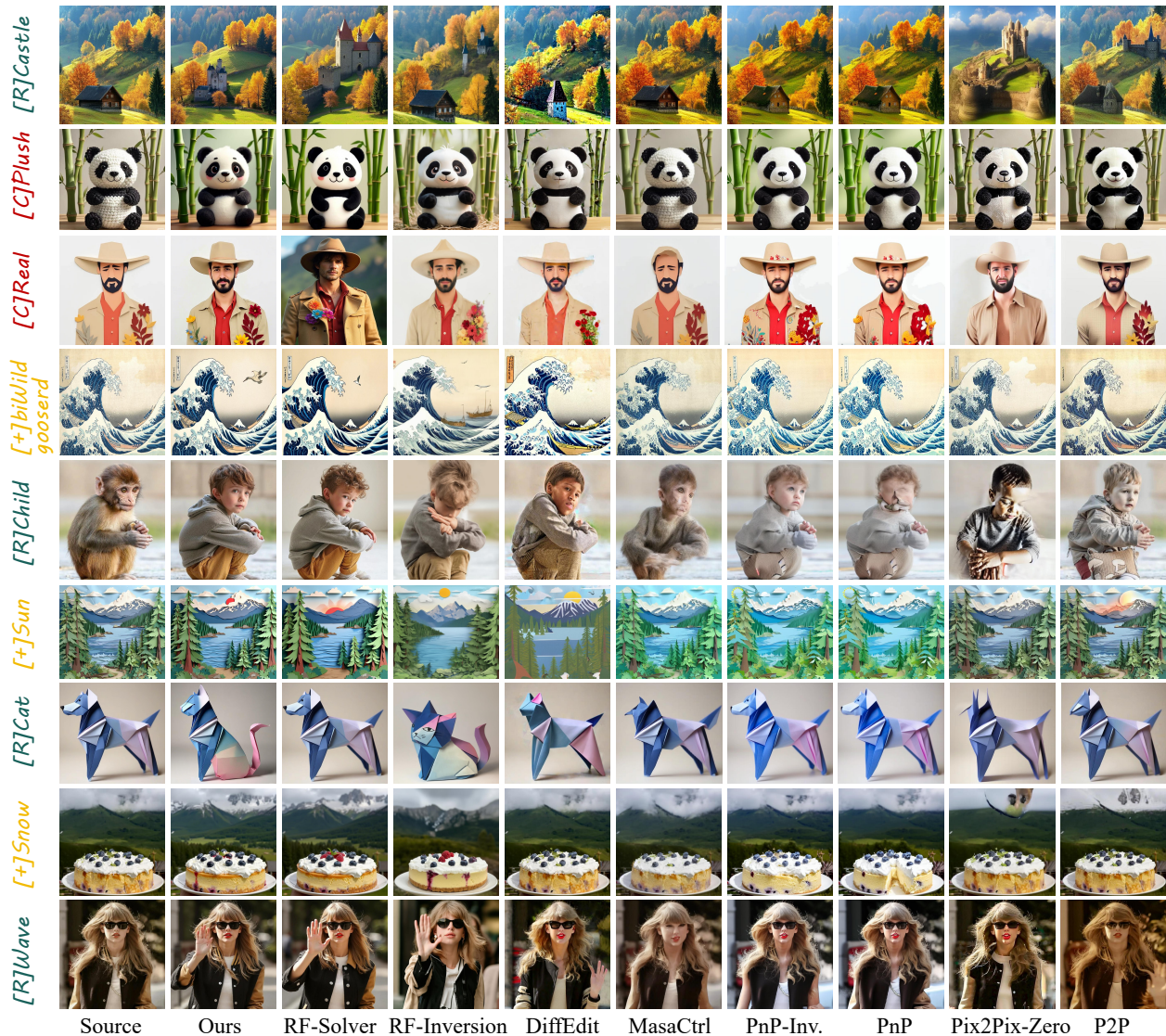


Figure 6. Comparison with State-of-the-art editing methods.

**Inference Speed:** In Table 5, we compare the inference time of FireFlow with several recent models. The number of steps is based on those reported in the original papers or provided in open-source code. FireFlow is significantly faster than competing reflow models and does not require an auxiliary model for editing.

## 6. Conclusion

We proposed a novel numerical solver for ReFlow models, achieving second-order precision at the computational cost of a first-order method. By reusing intermediate velocity approximations, our training-free approach fully exploits the nearly constant velocity dynamics of well-trained ReFlow models, minimizing computational overhead while maintaining accuracy and stability. This method addresses

key limitations of existing inversion techniques, providing a scalable and efficient solution for tasks such as image reconstruction and semantic editing. Our work highlights the untapped potential of ReFlow-based generative frameworks and establishes a foundation for further advancements in efficient numerical methods for generative ODEs. We also provide a discussion of the limitations in Section F.

## References

- Brack, M., Friedrich, F., Kornmeier, K., Tsuban, L., Schramowski, P., Kersting, K., and Passos, A. LED-ITS++: limitless image editing using text-to-image models. In *IEEE/CVF Conference on Computer Vision and Pattern Recognition, CVPR 2024, Seattle, WA, USA, June 16-22, 2024*, pp. 8861–8870. IEEE, 2024.



- Brooks, T., Holynski, A., and Efros, A. A. Instruct-pix2pix: Learning to follow image editing instructions. In *IEEE/CVF Conference on Computer Vision and Pattern Recognition, CVPR 2023, Vancouver, BC, Canada, June 17-24, 2023*, pp. 18392–18402. IEEE, 2023.
- Cao, M., Wang, X., Qi, Z., Shan, Y., Qie, X., and Zheng, Y. Masactrl: Tuning-free mutual self-attention control for consistent image synthesis and editing. In *Proceedings of the IEEE/CVF International Conference on Computer Vision (ICCV)*, pp. 22560–22570, October 2023.
- Chen, T., Gu, J., Dinh, L., Theodorou, E., Susskind, J. M., and Zhai, S. Generative modeling with phase stochastic bridge. In *The Twelfth International Conference on Learning Representations, 2024*. URL <https://openreview.net/forum?id=tUtGjQEDd4>.
- Chen, X., Fang, H., Lin, T., Vedantam, R., Gupta, S., Dollár, P., and Zitnick, C. L. Microsoft COCO captions: Data collection and evaluation server. *CoRR*, abs/1504.00325, 2015. URL <http://arxiv.org/abs/1504.00325>.
- Cho, H., Lee, J., Kim, S. B., Oh, T., and Jeong, Y. Noise map guidance: Inversion with spatial context for real image editing. In *The Twelfth International Conference on Learning Representations, ICLR 2024, Vienna, Austria, May 7-11, 2024*. OpenReview.net, 2024.
- Couairon, G., Verbeek, J., Schwenk, H., and Cord, M. Diffedit: Diffusion-based semantic image editing with mask guidance. In *The Eleventh International Conference on Learning Representations, ICLR 2023, Kigali, Rwanda, May 1-5, 2023*. OpenReview.net, 2023a.
- Couairon, G., Verbeek, J., Schwenk, H., and Cord, M. Diffedit: Diffusion-based semantic image editing with mask guidance. In *The Eleventh International Conference on Learning Representations, 2023b*. URL <https://openreview.net/forum?id=3lge0p5o-M->.
- Deutch, G., Gal, R., Garibi, D., Patashnik, O., and Cohen-Or, D. Turboedit: Text-based image editing using few-step diffusion models. In Igarashi, T., Shamir, A., and Zhang, H. R. (eds.), *SIGGRAPH Asia 2024 Conference Papers, SA 2024, Tokyo, Japan, December 3-6, 2024*, pp. 41:1–41:12. ACM, 2024.
- Dong, W., Xue, S., Duan, X., and Han, S. Prompt tuning inversion for text-driven image editing using diffusion models. In *IEEE/CVF International Conference on Computer Vision, ICCV 2023, Paris, France, October 1-6, 2023*, pp. 7396–7406. IEEE, 2023.
- Forest, B. Flux. <https://github.com/black-forest-labs/flux>. Accessed: [2024.12.8].
- Hertz, A., Mokady, R., Tenenbaum, J., Aberman, K., Pritch, Y., and Cohen-Or, D. Prompt-to-prompt image editing with cross attention control. *arXiv preprint arXiv:2208.01626*, 2022.
- Heusel, M., Ramsauer, H., Unterthiner, T., Nessler, B., and Hochreiter, S. Gans trained by a two time-scale update rule converge to a local nash equilibrium. In Guyon, I., von Luxburg, U., Bengio, S., Wallach, H. M., Fergus, R., Vishwanathan, S. V. N., and Garnett, R. (eds.), *Advances in Neural Information Processing Systems 30: Annual Conference on Neural Information Processing Systems 2017, December 4-9, 2017, Long Beach, CA, USA*, pp. 6626–6637, 2017.
- Huberman-Spiegelglas, I., Kulikov, V., and Michaeli, T. An edit friendly DDPM noise space: Inversion and manipulations. In *IEEE/CVF Conference on Computer Vision and Pattern Recognition, CVPR 2024, Seattle, WA, USA, June 16-22, 2024*, pp. 12469–12478. IEEE, 2024.
- Ju, X., Zeng, A., Bian, Y., Liu, S., and Xu, Q. Pnp inversion: Boosting diffusion-based editing with 3 lines of code. *International Conference on Learning Representations (ICLR)*, 2024.
- Lin, H., Wang, M., Wang, J., An, W., Chen, Y., Liu, Y., Tian, F., Dai, G., Wang, J., and Wang, Q. Schedule your edit: A simple yet effective diffusion noise schedule for image editing. *CoRR*, abs/2410.18756, 2024.
- Liu, X., Gong, C., and Liu, Q. Flow straight and fast: Learning to generate and transfer data with rectified flow. In *The Eleventh International Conference on Learning Representations, ICLR 2023, Kigali, Rwanda, May 1-5, 2023*. OpenReview.net, 2023. URL <https://openreview.net/forum?id=XVjTT1nw5z>.
- Meng, C., He, Y., Song, Y., Song, J., Wu, J., Zhu, J.-Y., and Ermon, S. SDEdit: Guided image synthesis and editing with stochastic differential equations. In *International Conference on Learning Representations, 2022*.
- Miyake, D., Iohara, A., Saito, Y., and Tanaka, T. Negative-prompt inversion: Fast image inversion for editing with text-guided diffusion models. *CoRR*, abs/2305.16807, 2023.
- Mokady, R., Hertz, A., Aberman, K., Pritch, Y., and Cohen-Or, D. Null-text inversion for editing real images using guided diffusion models. In *IEEE/CVF Conference on Computer Vision and Pattern Recognition, CVPR 2023, Vancouver, BC, Canada, June 17-24, 2023*, pp. 6038–6047. IEEE, 2023.
- Park, D., Lee, S., Kim, S., Lee, T., Hong, Y., and Kim, H. J. Constant acceleration flow. In *The Thirty-eighth Annual*

- Conference on Neural Information Processing Systems*, 2024. URL <https://openreview.net/forum?id=hsgNvC5YM9>.
- Parmar, G., Singh, K. K., Zhang, R., Li, Y., Lu, J., and Zhu, J. Zero-shot image-to-image translation. In Brunvand, E., Sheffer, A., and Wimmer, M. (eds.), *ACM SIGGRAPH 2023 Conference Proceedings, SIGGRAPH 2023, Los Angeles, CA, USA, August 6-10, 2023*, pp. 11:1–11:11. ACM, 2023. doi: 10.1145/3588432.3591513. URL <https://doi.org/10.1145/3588432.3591513>.
- Podell, D., English, Z., Lacey, K., Blattmann, A., Dockhorn, T., Müller, J., Penna, J., and Rombach, R. SDXL: Improving latent diffusion models for high-resolution image synthesis. In *The Twelfth International Conference on Learning Representations*, 2024. URL <https://openreview.net/forum?id=di52zR8xgf>.
- Radford, A., Kim, J. W., Hallacy, C., Ramesh, A., Goh, G., Agarwal, S., Sastry, G., Askell, A., Mishkin, P., Clark, J., Krueger, G., and Sutskever, I. Learning transferable visual models from natural language supervision. In Meila, M. and Zhang, T. (eds.), *Proceedings of the 38th International Conference on Machine Learning, ICML 2021, 18-24 July 2021, Virtual Event*, volume 139 of *Proceedings of Machine Learning Research*, pp. 8748–8763. PMLR, 2021.
- Ramesh, A., Dhariwal, P., Nichol, A., Chu, C., and Chen, M. Hierarchical text-conditional image generation with CLIP latents. *CoRR*, abs/2204.06125, 2022. doi: 10.48550/ARXIV.2204.06125. URL <https://doi.org/10.48550/arXiv.2204.06125>.
- Rombach, R., Blattmann, A., Lorenz, D., Esser, P., and Ommer, B. High-resolution image synthesis with latent diffusion models. In *Proceedings of the IEEE/CVF Conference on Computer Vision and Pattern Recognition (CVPR)*, pp. 10684–10695, June 2022.
- Rout, L., Chen, Y., Ruiz, N., Caramanis, C., Shakkottai, S., and Chu, W.-S. Semantic image inversion and editing using rectified stochastic differential equations. *arXiv preprint arXiv:2410.10792*, 2024.
- Song, J., Meng, C., and Ermon, S. Denoising diffusion implicit models. In *9th International Conference on Learning Representations, ICLR 2021, Virtual Event, Austria, May 3-7, 2021*. OpenReview.net, 2021.
- Tewel, Y., Gal, R., Samuel, D., Atzmon, Y., Wolf, L., and Chechik, G. Add-it: Training-free object insertion in images with pretrained diffusion models. *arXiv preprint arXiv:2411.07232*, 2024.
- Tumanyan, N., Geyer, M., Bagon, S., and Dekel, T. Plug-and-play diffusion features for text-driven image-to-image translation. In *IEEE/CVF Conference on Computer Vision and Pattern Recognition, CVPR 2023, Vancouver, BC, Canada, June 17-24, 2023*, pp. 1921–1930. IEEE, 2023a.
- Tumanyan, N., Geyer, M., Bagon, S., and Dekel, T. Plug-and-play diffusion features for text-driven image-to-image translation. In *IEEE/CVF Conference on Computer Vision and Pattern Recognition, CVPR 2023, Vancouver, BC, Canada, June 17-24, 2023*, pp. 1921–1930. IEEE, 2023b. doi: 10.1109/CVPR52729.2023.00191. URL <https://doi.org/10.1109/CVPR52729.2023.00191>.
- Urbanek, J., Bordes, F., Astolfi, P., Williamson, M., Sharma, V., and Romero-Soriano, A. A picture is worth more than 77 text tokens: Evaluating clip-style models on dense captions. In *Proceedings of the IEEE/CVF Conference on Computer Vision and Pattern Recognition (CVPR)*, pp. 26700–26709, June 2024.
- Wang, J., Pu, J., Qi, Z., Guo, J., Ma, Y., Huang, N., Chen, Y., Li, X., and Shan, Y. Taming rectified flow for inversion and editing. *arXiv preprint arXiv:2411.04746*, 2024.
- Wang, Z., Bovik, A. C., Sheikh, H. R., and Simoncelli, E. P. Image quality assessment: from error visibility to structural similarity. *IEEE Trans. Image Process.*, 13(4): 600–612, 2004.
- Xu, S., Huang, Y., Pan, J., Ma, Z., and Chai, J. Inversion-free image editing with natural language. 2024.
- Zhang, R., Isola, P., Efros, A. A., Shechtman, E., and Wang, O. The unreasonable effectiveness of deep features as a perceptual metric. In *2018 IEEE Conference on Computer Vision and Pattern Recognition, CVPR 2018, Salt Lake City, UT, USA, June 18-22, 2018*, pp. 586–595. Computer Vision Foundation / IEEE Computer Society, 2018.
- Zhang, Y., Huang, N., Tang, F., Huang, H., Ma, C., Dong, W., and Xu, C. Inversion-based creativity transfer with diffusion models. *CoRR*, abs/2211.13203, 2022.

## A. The Pseudo-code for Inversion and Editing

---

### Algorithm 1 Solving ReFlow Inversion ODE

---

**Require:** Discretization steps  $N$ , reference image  $X_0$ , prompt embedding network  $\Phi$ , Flux model  $v(\cdot, \cdot, \cdot; \varphi)$ , time steps  $t = [t_0, \dots, t_{N-1}]$

**Ensure:** Structured noise  $X_1$

- 1: Initialize  $v_{t_0}(X_{t_0}) = v(X_{t_0}, t_0, \Phi(\cdot); \varphi)$  {Run}
- 2:  $\Delta t_0 = t_1 - t_0$
- 3:  $X_{t_0 + \frac{1}{2}\Delta t_0} = X_{t_0} + \frac{1}{2}\Delta t_0 \cdot v_{t_0}(X_{t_0})$
- 4: Initialize  $v_{t_0 + \frac{1}{2}\Delta t_0}(X_{t_0 + \frac{1}{2}\Delta t_0}) = v(X_{t_0 + \frac{1}{2}\Delta t_0}, t_0 + \frac{1}{2}\Delta t_0, \Phi(\cdot); \varphi)$  {Run & Save to GPU Memory}
- 5:  $X_{t_1} = X_{t_0} + \Delta t_0 \cdot v_{t_0 + \frac{1}{2}\Delta t_0}(X_{t_0 + \frac{1}{2}\Delta t_0})$
- 6: **for**  $i = 1 : N - 1$  **do**
- 7:  $\hat{v}_{t_i}(X_{t_i}) \leftarrow v_{t_{i-1} + \frac{1}{2}\Delta t_{i-1}}(X_{t_{i-1} + \frac{1}{2}\Delta t_{i-1}})$  {Load from GPU Memory}
- 8:  $\Delta t_i = t_{i+1} - t_i$
- 9:  $X_{t_i + \frac{1}{2}\Delta t_i} = X_{t_i} + \frac{1}{2}\Delta t_i \cdot \hat{v}_{t_i}(X_{t_i})$
- 10:  $v_{t_i + \frac{1}{2}\Delta t_i}(X_{t_i + \frac{1}{2}\Delta t_i}) = v(X_{t_i + \frac{1}{2}\Delta t_i}, t_i + \frac{1}{2}\Delta t_i, \Phi(\cdot); \varphi)$  {Run & Save to GPU Memory}
- 11:  $X_{t_{i+1}} = X_{t_i} + \Delta t_i \cdot v_{t_i + \frac{1}{2}\Delta t_i}(X_{t_i + \frac{1}{2}\Delta t_i})$
- 12: **if**  $i == N - 1$  **then**
- 12:     Save  $V_{t_{N-1}}^{inv.}$  to storage.
- 13: **end if**
- 14: **end for**
- 15: **return**  $X_1, V_{t_{N-1}}^{inv.}$  in Self-attention Layers

---

### Algorithm 2 Solving ReFlow Denoising ODE (Editing)

---

**Require:** Discretization steps  $N$ , reference text "prompt", structured noise  $X_1$ , prompt embedding network  $\Phi$ , Flux model  $v(\cdot, \cdot, \cdot; \varphi)$ , time steps  $t = [t_{N-1}, \dots, t_0]$ , pre-computed  $V_{t_{N-1}}^{inv.}$  in Self-attention Layers during inversion

**Ensure:** Edited image  $X_0$

- 1: Initialize  $v_{t_{N-1}}(X_{t_{N-1}}) = v(X_{t_{N-1}}, t_{N-1}, \Phi(\text{prompt}); \varphi)$  {Replace  $V_{t_{N-1}}^{edit}$  with  $V_{t_{N-1}}^{inv.}$  in Self-attention & Run}
- 2:  $\Delta t_{N-1} = t_{N-2} - t_{N-1}$
- 3:  $X_{t_{N-1} + \frac{1}{2}\Delta t_{N-1}} = X_{t_{N-1}} + \frac{1}{2}\Delta t_{N-1} \cdot v_{t_{N-1}}(X_{t_{N-1}})$
- 4: Initialize  $v_{t_{N-1} + \frac{1}{2}\Delta t_{N-1}}(X_{t_{N-1} + \frac{1}{2}\Delta t_{N-1}}) = v(X_{t_{N-1} + \frac{1}{2}\Delta t_{N-1}}, t_{N-1} + \frac{1}{2}\Delta t_{N-1}, \Phi(\text{prompt}); \varphi)$  {Replace  $V_{t_{N-1}}^{edit}$  with  $V_{t_{N-1}}^{inv.}$  in Self-attention & Run & Save to GPU Memory}
- 5:  $X_{t_{N-2}} = X_{t_{N-1}} + \Delta t_{N-1} \cdot v_{t_{N-1} + \frac{1}{2}\Delta t_{N-1}}(X_{t_{N-1} + \frac{1}{2}\Delta t_{N-1}})$
- 6: **for**  $i = N - 2 : 0$  **do**
- 7:  $\hat{v}_{t_i}(X_{t_i}) \leftarrow v_{t_{i+1} + \frac{1}{2}\Delta t_{i+1}}(X_{t_{i+1} + \frac{1}{2}\Delta t_{i+1}})$  {Load from GPU Memory}
- 8:  $\Delta t_i = t_{i-1} - t_i$
- 9:  $X_{t_i + \frac{1}{2}\Delta t_i} = X_{t_i} + \frac{1}{2}\Delta t_i \cdot \hat{v}_{t_i}(X_{t_i})$
- 10:  $v_{t_i + \frac{1}{2}\Delta t_i}(X_{t_i + \frac{1}{2}\Delta t_i}) = v(X_{t_i + \frac{1}{2}\Delta t_i}, t_i + \frac{1}{2}\Delta t_i, \Phi(\text{prompt}); \varphi)$  {Run & Save to GPU Memory}
- 11:  $X_{t_{i-1}} = X_{t_i} + \Delta t_i \cdot v_{t_i + \frac{1}{2}\Delta t_i}(X_{t_i + \frac{1}{2}\Delta t_i})$
- 12: **end for**
- 13: **return**  $X_0$

---

## B. Technical Proofs

This section provides detailed technical proofs for the theoretical results discussed in this paper.

### B.1. Proof of Proposition 3.1

*Proof.* The reverse ODE is given by:

$$\frac{dx}{dt} = -v(x, t). \quad (13)$$

Let  $x^{\text{True}}(t)$  be the true solution of the reverse ODE, starting from  $x_T^{\text{True}}$ , and  $x^{\text{Perturbed}}(t)$  be the solution starting from  $x_T^{\text{Numerical}} = x_T^{\text{True}} + \Delta_T$ . The initial condition difference is:

$$x_T^{\text{Perturbed}}(T) - x_T^{\text{True}}(T) = \Delta_T. \quad (14)$$

Define the error  $\Delta(t)$  as the difference between the perturbed and true solutions:

$$\Delta(t) = x^{\text{Perturbed}}(t) - x^{\text{True}}(t). \quad (15)$$

The dynamics of  $\Delta(t)$  follow from the reverse ODE:

$$\frac{d\Delta(t)}{dt} = \frac{dx^{\text{Perturbed}}(t)}{dt} - \frac{dx^{\text{True}}(t)}{dt}. \quad (16)$$

Substituting the reverse ODE for each term:

$$\frac{d\Delta(t)}{dt} = -v(x^{\text{Perturbed}}(t), t) + v(x^{\text{True}}(t), t). \quad (17)$$

Using the Lipschitz continuity of  $v(x, t)$ , we have:

$$\|v(x^{\text{Perturbed}}(t), t) - v(x^{\text{True}}(t), t)\| \leq L\|\Delta(t)\|, \quad (18)$$

where  $L$  is the Lipschitz constant of  $v(x, t)$ . Thus,

$$\left\| \frac{d\Delta(t)}{dt} \right\| \leq L\|\Delta(t)\|. \quad (19)$$

Based on the definition of the derivative of a norm:

$$\frac{d\|\Delta(t)\|}{dt} = \frac{\Delta(t)}{\|\Delta(t)\|} \cdot \frac{d\Delta(t)}{dt} \leq \left\| \frac{\Delta(t)}{\|\Delta(t)\|} \right\| \cdot \left\| \frac{d\Delta(t)}{dt} \right\| = \left\| \frac{d\Delta(t)}{dt} \right\| \leq L\|\Delta(t)\|, \quad (20)$$

This can be rewritten as:

$$\frac{d\|\Delta(t)\|}{\|\Delta(t)\|} \leq L dt. \quad (21)$$

Integrate both sides from  $t = T$  (initial condition) to  $t = 0$  (final condition):

$$\int_T^0 \frac{d\|\Delta(t)\|}{\|\Delta(t)\|} \leq \int_T^0 L dt. \quad (22)$$

Thus, the inequality becomes:

$$\ln \|\Delta(0)\| - \ln \|\Delta(T)\| \leq -LT. \quad (23)$$

Simplify:

$$\ln \|\Delta(0)\| \leq \ln \|\Delta(T)\| - LT. \quad (24)$$

Exponentiate both sides to remove the logarithm:

$$\|\Delta(0)\| \leq \|\Delta(T)\|e^{-LT}. \quad (25)$$

□

## B.2. Proof of Proposition 4.1

*Proof.* Define the time interval between  $t$  and  $t - 1$  as  $\Delta t$  for simplicity, the reused velocity at  $t$  is given by:

$$\hat{v}_\theta(X_t, t) = v_\theta(X_{(t-1)+\frac{\Delta t}{2}}, (t-1) + \frac{\Delta t}{2}), \quad (26)$$

where  $X_{(t-1)+\frac{\Delta t}{2}}$  is computed recursively using:

$$X_{(t-1)+\frac{\Delta t}{2}} = X_{t-1} + \frac{\Delta t}{2} \hat{v}_\theta(X_{t-1}, t-1). \quad (27)$$

The exact velocity at  $t$  is:

$$v_\theta(X_t, t). \quad (28)$$

To quantify the difference  $\|\hat{v}_\theta(X_t, t) - v_\theta(X_t, t)\|$ , we expand the reused velocity  $\hat{v}_\theta(X_t, t)$  around the exact velocity  $v_\theta(X_t, t)$ . Using a Taylor series expansion, expand  $v_\theta(X_{(t-1)+\frac{\Delta t}{2}}, (t-1) + \frac{\Delta t}{2})$  around  $X_t$  and  $t$ :

$$v_\theta(X_{(t-1)+\frac{\Delta t}{2}}, (t-1) + \frac{\Delta t}{2}) \approx v_\theta(X_t, t) + \frac{\partial v_\theta}{\partial X}(X_{(t-1)+\frac{\Delta t}{2}} - X_t) + \frac{\partial v_\theta}{\partial t}(-\Delta t + \frac{\Delta t}{2}) + \mathcal{O}(\Delta t^2). \quad (29)$$

The temporal difference is:

$$-\Delta t + \frac{\Delta t}{2} = \frac{-\Delta t}{2}. \quad (30)$$

Thus, the temporal contribution to the velocity difference is:

$$-\frac{\Delta t}{2} \frac{\partial v_\theta}{\partial t}. \quad (31)$$

The leading term introduces an error of  $\mathcal{O}(\Delta t)$ .

The spatial difference is:

$$X_{(t-1)+\frac{\Delta t}{2}} - X_t. \quad (32)$$

Using the recursive relationship:

$$X_{(t-1)+\frac{\Delta t}{2}} = X_{t-1} + \frac{\Delta t}{2} \hat{v}_\theta(X_{t-1}, t-1), \quad (33)$$

and the local truncation error of Euler method

$$X_t \approx X_{t-1} + \Delta t \cdot v_\theta(X_{t-1}, t-1) + \mathcal{O}(\Delta t^2), \quad (34)$$

we subtract:

$$X_{(t-1)+\frac{\Delta t}{2}} - X_t = -\Delta t \cdot v_\theta(X_{t-1}, t-1) + \frac{\Delta t}{2} \hat{v}_\theta(X_{t-1}, t-1) + \mathcal{O}(\Delta t^2). \quad (35)$$

Simplify:

$$X_{(t-1)+\frac{\Delta t}{2}} - X_t = \frac{\Delta t}{2} (\hat{v}_\theta(X_{t-1}, t-1) - 2 \cdot v_\theta(X_{t-1}, t-1)) + \mathcal{O}(\Delta t^2). \quad (36)$$

Substitute this into the spatial term:

$$\frac{\partial v_\theta}{\partial X}(X_{(t-1)+\frac{\Delta t}{2}} - X_t) = \frac{\Delta t}{2} \frac{\partial v_\theta}{\partial X} (\hat{v}_\theta(X_{t-1}, t-1) - 2 \cdot v_\theta(X_{t-1}, t-1)) + \mathcal{O}(\Delta t^2). \quad (37)$$

Combine both temporal and spatial difference:

$$\hat{v}_\theta(X_t, t) - v_\theta(X_t, t) = \frac{\Delta t}{2} \frac{\partial v_\theta}{\partial X} (\hat{v}_\theta(X_{t-1}, t-1) - v_\theta(X_{t-1}, t-1)) - \frac{\Delta t}{2} \left( \frac{\partial v_\theta}{\partial t} + \frac{\partial v_\theta}{\partial X} v_\theta(X_{t-1}, t-1) \right) + \mathcal{O}(\Delta t^2). \quad (38)$$

Let  $\delta_t = \|\hat{v}_\theta(X_t, t) - v_\theta(X_t, t)\|$ . From the above analysis and triangle inequality:

$$\delta_t \leq \frac{\Delta t}{2} \delta_{t-1} + \mathcal{O}(\Delta t). \quad (39)$$

Unfold the recursion:

$$\delta_t \leq \mathcal{O}(\Delta t) + \frac{\Delta t}{2} \mathcal{O}(\Delta t) + \left( \frac{\Delta t}{2} \right)^2 \mathcal{O}(\Delta t) + \dots. \quad (40)$$

This is a geometric series with common ratio  $\frac{\Delta t}{2}$ , summing to:

$$\delta_t \leq \mathcal{O}(\Delta t) \cdot \sum_{k=0}^{\infty} \left( \frac{\Delta t}{2} \right)^k = \mathcal{O}(\Delta t) \cdot \frac{1}{1 - \frac{\Delta t}{2}}. \quad (41)$$

For small  $\Delta t$ ,  $\frac{1}{1 - \frac{\Delta t}{2}} \approx 1 + \frac{\Delta t}{2}$ , so:

$$\delta_t = \|\hat{v}_\theta(X_t, t) - v_\theta(X_t, t)\| \leq \mathcal{O}(\Delta t). \quad (42)$$

□

### B.3. Proof of Theorem 4.2

*Proof.* Define the time interval as  $\Delta t$  for simplicity, our modified midpoint method updates  $X_{t+1}$  as:

$$X_{t+1} = X_t + \Delta t \cdot v_\theta(X_{t+\frac{\Delta t}{2}}, t + \frac{\Delta t}{2}), \quad (43)$$

where:

$$X_{t+\frac{\Delta t}{2}} = X_t + \frac{\Delta t}{2} \hat{v}_\theta(X_t, t). \quad (44)$$

Substituting  $X_{t+\frac{\Delta t}{2}}$ , the velocity term becomes:

$$v_\theta(X_{t+\frac{\Delta t}{2}}, t + \frac{\Delta t}{2}) \approx v_\theta(X_t, t) + \frac{\Delta t}{2} \frac{\partial v_\theta}{\partial t} + \frac{\Delta t}{2} \frac{\partial v_\theta}{\partial X} \hat{v}_\theta(X_t, t) + \mathcal{O}(\Delta t^2). \quad (45)$$

Under the assumption  $\|\hat{v}_\theta(X_t, t) - v_\theta(X_t, t)\| \leq \mathcal{O}(\Delta t)$ , we write:

$$\hat{v}_\theta(X_t, t) = v_\theta(X_t, t) + \delta v, \quad (46)$$

where  $\|\delta v\| \leq \mathcal{O}(\Delta t)$ . Substituting this into the velocity term expansion:

$$\frac{\partial v_\theta}{\partial X} \hat{v}_\theta(X_t, t) = \frac{\partial v_\theta}{\partial X} v_\theta(X_t, t) + \frac{\partial v_\theta}{\partial X} \delta v. \quad (47)$$

Since  $\|\delta v\| \leq \mathcal{O}(\Delta t)$ , the additional term  $\frac{\Delta t}{2} \cdot \frac{\partial v_\theta}{\partial X} \delta v$  contributes an error of  $\mathcal{O}(\Delta t^2)$ , which is of the same order as higher-order terms in the expansion. Thus, the velocity term becomes:

$$v_\theta(X_{t+\frac{\Delta t}{2}}, t + \frac{\Delta t}{2}) \approx v_\theta(X_t, t) + \frac{\Delta t}{2} \frac{\partial v_\theta}{\partial t} + \frac{\Delta t}{2} \frac{\partial v_\theta}{\partial X} v_\theta(X_t, t) + \mathcal{O}(\Delta t^2). \quad (48)$$

Substituting the expanded velocity back into the update equation:

$$X_{t+1} = X_t + \Delta t \cdot \left( v_\theta(X_t, t) + \frac{\Delta t}{2} \frac{\partial v_\theta}{\partial t} + \frac{\Delta t}{2} \frac{\partial v_\theta}{\partial X} v_\theta(X_t, t) + \mathcal{O}(\Delta t^2) \right). \quad (49)$$

Simplify:

$$X_{t+1} = X_t + \Delta t \cdot v_\theta(X_t, t) + \frac{\Delta t^2}{2} \frac{\partial v_\theta}{\partial t} + \frac{\Delta t^2}{2} \frac{\partial v_\theta}{\partial X} v_\theta(X_t, t) + \mathcal{O}(\Delta t^3). \quad (50)$$

The exact solution to the ODE is:

$$X(t + \Delta t) = X(t) + \Delta t \cdot v_\theta(X_t, t) + \frac{\Delta t^2}{2} \frac{\partial v_\theta}{\partial t} + \frac{\Delta t^2}{2} \frac{\partial v_\theta}{\partial X} v_\theta(X_t, t) + \mathcal{O}(\Delta t^3). \quad (51)$$

The modified midpoint method's update matches the exact solution up to  $\mathcal{O}(\Delta t^2)$ , confirming that the local truncation error remains  $\mathcal{O}(\Delta t^3)$ . Since the local truncation error is  $\mathcal{O}(\Delta t^3)$ , the global error accumulates over  $\mathcal{O}(1/\Delta t)$  steps, resulting in  $\mathcal{O}(\Delta t^2)$ .  $\square$

## C. Empirical Convergence Rate

In this section, we present the reconstruction errors of various methods with NFE up to 60. Our approach demonstrates rapid convergence, achieving consistently low reconstruction error upon full convergence to the minimum value. In contrast, vanilla ReFlow with the first-order Euler method exhibits a slow convergence rate, while RF-solver with a second-order truncation error shows an error increase after convergence, with optimal performance observed at around 25 steps.

## D. Python-style Pseudo-Code

In this section, we present Python-style pseudo-code to illustrate the core concept of our approach, which is remarkably simple yet delivers promising results. Except for the first iteration, where  $\hat{v}$  is initialized as None, subsequent iterations require only a single function call for model evaluation, matching the computational cost of the original ReFlow model (i.e., the Euler method). However, as shown in Figure 7, the convergence rate of our approach is significantly faster than that of the vanilla first-order method.

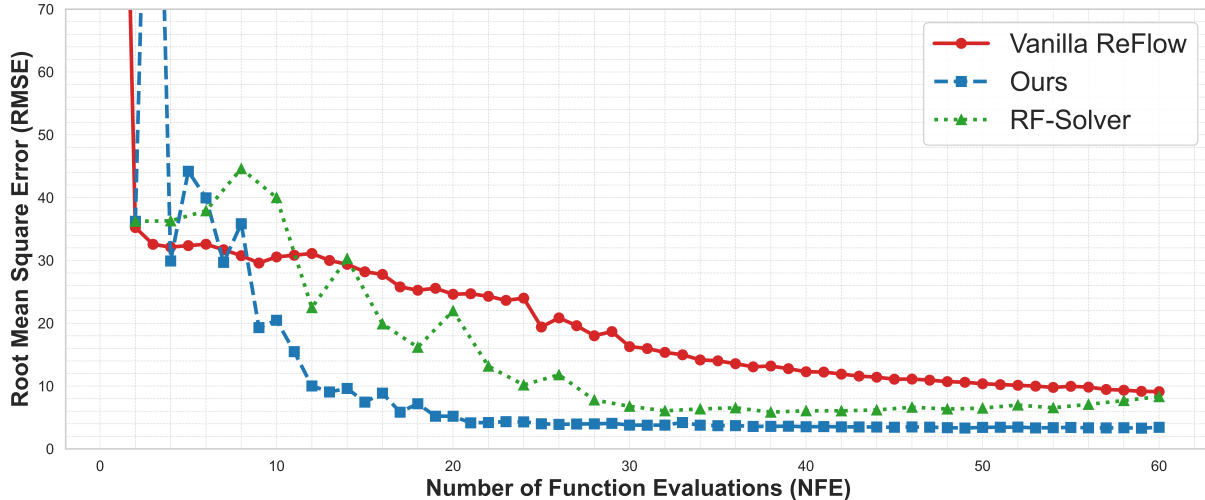


Figure 7. Visualization of the convergence rate of different order inversion and reconstruction method. With 60 NFE, our approach still enjoys the lowest reconstruction error and the fast convergence speed.

Table 6. Comparison on different editing methods. Results on PIE Bench are reported. Guidance terms indicate the guidance ratio settings used in the FLUX model during the denoising process.

Method	Guidance	Structure	Background Preservation		CLIP Similarity $\uparrow$		Steps	NFE $\downarrow$
		Distance $\downarrow$	PSNR $\uparrow$	SSIM $\uparrow$	Whole	Edited		
Add $Q$	[1,2,2,...]	0.0590	17.72	0.7340	27.01	23.84	<b>8</b>	<b>18</b>
Add $Q$ + Add $K$	[1,2,2,...]	0.0537	18.35	0.7520	26.82	23.60	<b>8</b>	<b>18</b>
Add $Q$ + Add $K$ + Add $V$	[1,2,2,...]	0.0416	19.63	0.7805	25.95	22.92	<b>8</b>	<b>18</b>
Add $Q$	[1,1,2,...]	0.0530	18.78	0.7580	26.99	23.85	15	32
Add $Q$ + Add $K$	[1,1,2,...]	0.0486	19.30	0.7721	26.68	23.59	15	32
Replace $V$	[2,...]	<b>0.0271</b>	<b>23.03</b>	<b>0.8249</b>	26.02	22.81	<b>8</b>	<b>18</b>
Add $Q$	[2,...]	0.0710	16.49	0.7077	<b>27.33</b>	<b>24.09</b>	<b>8</b>	<b>18</b>
Add $K$	[2,...]	0.0738	16.41	0.7066	27.25	24.01	<b>8</b>	<b>18</b>

```

1 hat_velocity = None
2 for t_curr, t_prev in zip(timesteps[:-1], timesteps[1:]):
3     if hat_velocity is None:
4         velocity = model(X, t_curr)
5     else:
6         velocity = hat_velocity
7     X_mid = X + (t_prev - t_curr) / 2 * velocity
8     velocity_mid = model(X_mid, t_curr + (t_prev - t_curr) / 2)
9     hat_velocity = velocity_mid
10    X = X + (t_prev - t_curr) * velocity_mid
11 return X
    
```

## E. Ablation Study

**Editing Steps** We conducted an ablation study by varying the number of editing steps from 2 to 12, as shown in Figure 8. The results reveal that at the 2-step setting, the editing prompts are less effective. However, as the number of steps increases, the editing performance improves significantly. The subject being edited with 8 steps are comparable to those with 10 or 12 steps, indicating that 8 steps are sufficient. Therefore, 8 steps are used in the subsequent experiments.

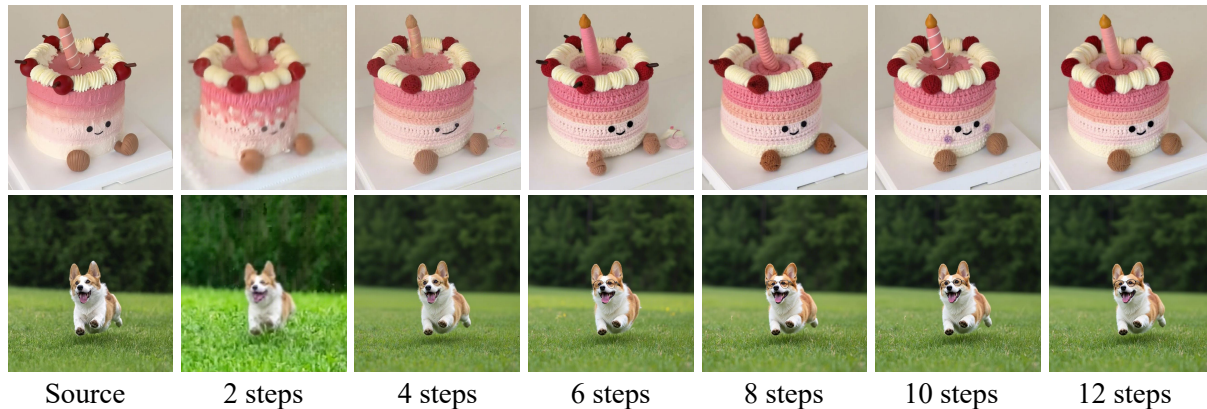


Figure 8. Ablation Study on the Number of Editing Steps.

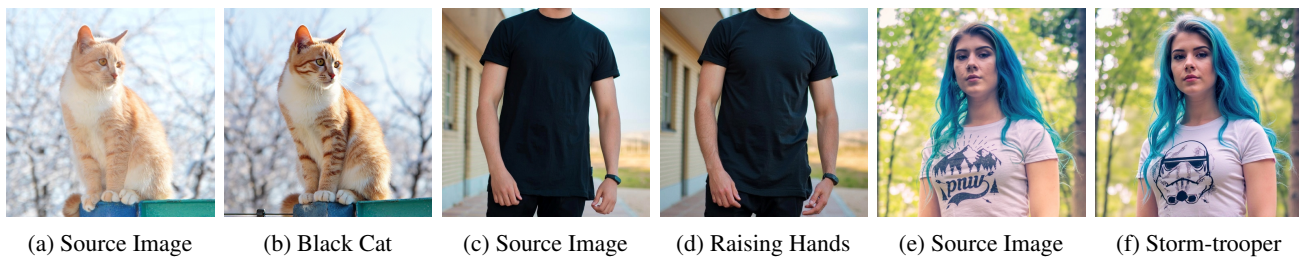


Figure 9. Illustrations on FireFlow Failure Cases.

## F. Limitations

We empirically observe that our approach struggles with editing tasks involving changes to object colors or uncommon scenarios in natural images. As illustrated in Figure 9, the cat’s color remains unsatisfactory after editing. Similarly, in less common scenes, such as when the person’s head is not visible in the image, the editing results are poor.

Another example involves an uncommon description, such as “a [stormtrooper] with blue hair wearing a shirt,” which also yields unexpected results. We attribute these issues to the simplicity of the editing strategy, which involves only replacing the  $V$  feature in the self-attention module. This approach appears insufficient for handling such scenarios.

We empirically find that incorporating  $K$  feature addition in the self-attention module can resolve these problems. Formally,

$$\text{Self\_Attn}_{edit} = \text{Softmax}\left(\frac{Q_{edit}(K_{edit} + K_{inv.})}{\sqrt{d}}\right)V_{edit} \tag{52}$$

However, this comes at the cost of diminished preservation of the original structure and background details. Details can be found in Figure 10. We also include an quantitative analysis on different editing strategies in Table 6. The results are consistent with the illustrations. It is evident that Equation 52 belongs to the category of “cross-attention,” focusing on merging features from the self-attention module during inversion with the corresponding features generated during the denoising process. This concept has been extensively discussed in diffusion model (DM) editing methods. Table 6 presents only the foundational attempts in this direction. We hope this will inspire further research and advancements in future work.





Figure 10. Illustrations on FireFlow with K feature addition in Self-attention.